Deterministic Model of AcousticWave Propagation in a Cavity

van Dercreek, Colin; Sijtsma, Pieter; Snellen, Mirjam; Ragni, Daniele; Avallone, Francesco; Simons, Dick

DOI
10.2514/6.2019-2425

Publication date
2019

Document Version
Final published version

Published in
25th AIAA/CEAS Aeroacoustics Conference

Aeroacoustics Conferences
20-23 May 2019, Delft, The Netherlands
25th AIAA/CEAS Aeroacoustics Conference

10.2514/6.2019-2425

Deterministic Model of Acoustic Wave Propagation in a Cavity

Colin P VanDercreek*
Delft University of Technology, 2629HS Delft, The Netherlands

Pieter Sijtsma†
PSA3, 8091AV Wezep, The Netherlands

Mirjam Snellen‡, Daniele Ragni§, Francesco Avallone¶, and Dick G. Simons‖
Delft University of Technology, 2629HS Delft, The Netherlands

A mathematical model is proposed that evaluates acoustic propagation of turbulent boundary layer waves on top of a cavity enclosing a microphone. The goal is to optimize these cavity geometries to improve the signal-to-noise ratio of acoustic measurements. This model predicts the attenuation of the turbulent boundary layer fluctuations propagating within the cavity for a given wind tunnel speed, porous surface resistance and cavity geometry. Duct acoustics predict that the spatial wave numbers of the turbulent boundary layer pressure fluctuations are shorter than the acoustic wavelength and are therefore evanescent in the cavity. These cavities are also covered with a porous material such as a metallic mesh or kevlar, to attenuate hydrodynamic fluctuations through the cavity. This model supports the investigation of 3D cylindrical cavities and incorporates both soft and hard cavity walls. Good agreement was found with experimental data.

I. Nomenclature

a	=	absolute radius of the cavity, m
$A^+_{m\mu}$	=	amplitude of inward propagating mode above mesh
$A^-_{m\mu}$	=	amplitude of inward propagating mode within the cavity
$B^+_{m\mu}$	=	amplitude of outward propagating mode above mesh
$B^-_{m\mu}$	=	amplitude of outward propagating mode within the cavity
c_0	=	speed of sound in air, m/sec
F	=	mode shape in the radial direction
G	=	mode shape in the circumferential direction
H	=	mode shape in the axial direction
i	=	$\sqrt{-1}$
$k_{m\mu}$	=	axial wave number
L	=	depth of cavity below mesh, m
$\tilde{L}$	=	normalized depth of cavity below mesh, $\tilde{L} = \frac{L}{a}$
m	=	azimuthal mode index
n	=	iteration index
p	=	acoustic pressure, Pa
$\tilde{p}$	=	normalized pressure, $\frac{p}{\rho_0 c_0^2}$
P	=	integrated pressure at $z = 0$

*Ph.D. Candidate, Aircraft Noise and Climate Effects (ANCE), Section, Faculty of Aerospace Engineering, Kluyverweg 1, c.p.vandercreek-1@tudelft.nl, Member AIAA

†Director, pieter.sijtsma@psa3.nl

‡Associate Professor, Aircraft Noise and Climate Effects (ANCE) Section, Faculty of Aerospace Engineering, Kluyverweg 1, M.Snellen@tudelft.nl

§Assistant Professor, Aerodynamics, Wind Energy, Flight Performance and Propulsion (AWEP), Department, Faculty of Aerospace Engineering, Kluyverweg 1, D.Ragni@tudelft.nl, Member AIAA

¶Assistant Professor, Aerodynamics, Wind Energy, Flight Performance and Propulsion (AWEP), Department, Faculty of Aerospace Engineering, Kluyverweg 1, F.Avallone@tudelft.nl, Member AIAA

‖Professor, Aircraft Noise and Climate Effects (ANCE) Section, Faculty of Aerospace Engineering, Kluyverweg 1, D.G.Simons@tudelft.nl

r = radius variable, m
$\tilde{r}$ = normalized radius variable, $\frac{r}{a}$
R = dimensionless acoustic resistance across porous sheet
Q = integrated pressure at the bottom of the cavity
$\tilde{t}$ = normalized time, $\frac{tc_0}{a}$
U_c = boundary layer convection speed, m/sec
v = acoustic velocity, m/sec
$\tilde{v}$ = normalized velocity, $\frac{v}{c_0}$
x_0 = wavelet reference position, m
$\tilde{z}$ = normalized propagation distance, $\frac{z}{a}$
Z = impedance
λ = constant
μ = radial mode order
ρ = acoustic air density, kg/m^3
$\tilde{\rho}$ = normalized density, $\frac{\rho}{\rho_0}$
ρ_0 = ambient air density
σ = wavelet expression constant
ω = angular frequency
$\tilde{\omega}$ = normalized angular frequency, $\frac{\omega a}{c_0}$

II. Introduction

Microphone arrays are used with beam-forming algorithms to localize and quantify aeroacoustic noise sources in wind tunnel or in-field tests. [1]. These arrays are either installed along the wall of a closed test section wind tunnel or outside of the free field of an open jet wind tunnel. Closed test-section wind tunnels are often preferable for aerodynamic measurements due to the reduction in jet deflection, blockage and non-zero circulation effects. However there is the possibility of more background noise due to reflections from the wind tunnel walls and contamination of the acoustic signal by the surface pressure fluctuations due to the boundary layer [2]. These undesirable sources of noise reduce the signal-to-noise ratio (SNR) of the acoustic measurements. One solution to reduce the contamination due to the surface pressure fluctuations is to recess the microphones in a cavity [3]. The working principle is that the shorter wavelengths associated with the turbulent boundary layer pressure waves attenuate quickly inside the cavity. These cavities are covered with an acoustically transparent cover to reduce the transmission of hydrodynamic pressure waves from the boundary layer. The goal of this research is to develop a deterministic model that quantifies the influence of different cavity geometries on the measured boundary layer pressure fluctuations at the base of the cavity.

The model described in this paper uses the principles of duct acoustics as a basis to better understand how cavities can be designed to reduce the propagation of turbulent boundary layer (TBL) hydrodynamic pressure fluctuations from the top of the cavity to the microphone at the base. A substantial body of research has been published describing how to model the propagation of waves in a duct [4, 5]. This work has a focus on modeling the acoustic modes in cavities and noise generated by flow over cavities.

A deterministic model, using duct modal propagation, is useful for evaluating how different cavity geometries affect the propagation of acoustic pressure waves to the bottom of the cavity. Previous work in this area has primarily focused on predicting cavity modes [6]. This insight will be leveraged to determine how parameters such as lining material and cavity shape reduce the amount of hydrodynamic energy from the boundary layer that the microphone measures. This type of model has the advantage of being less computationally expensive than a detailed computational fluid dynamics (CFD) simulation or computational aeroacoustics (CAA) simulation [7]. Additionally this approach provides insight into the underlying physics and acoustic propagation mechanisms, e.g. cut-off acoustic mode attenuation, by requiring careful consideration of how the acoustic waves propagate, reflect off of surfaces, and attenuate with propagation distance. The drawback to this approach is that modeling arbitrary geometries is more challenging as the boundary conditions for solving the wave equation need to be carefully considered and implemented [8].

The proposed acoustic cavity propagation model imposes a fluctuating pressure wave representing the boundary layer at the interface between the top of the three dimensional cavity and the mesh or porous covering. Several boundary layer pressure spectral models were evaluated including, a model based on the Corcos' [9], the Howe model [10], the Smol'yakov and Tkachenko model [11], and the Goody model [12]. The resulting boundary layer energy estimated by these models is dependent on the boundary layer properties and varies with frequency. In order to model a pressure

wave over the cavity, a finite coherence length was simulated using a wavelet expression with a finite support defined in terms of the boundary layer convection velocity and the distance traveled along the top of the cavity. This approximation was applied to all models. It is important to note that this model assumes that only acoustic waves are propagating within the cavity, and not the hydrodynamic wave component of the boundary layer.

Testing was performed at two wind tunnels to collect baseline data on the interaction between the tunnel boundary layer and different cavity geometries. Testing was performed in the Low Turbulence Tunnel (LTT) at the Delft University of Technology (TU Delft) [13] in The Netherlands and at the Deutsche WindGuard commercial tunnel in Bremerhaven, Germany. For these tests, microphones were placed flush with the tunnel wall and at the bottom of different cavity geometries. These data are used to validate the model.

III. Model Development

The goal of the model presented in this paper is to estimate the reduction in the transmitted energy from the boundary layer to the bottom of a cylindrical cavity. This model assumes three-dimensional acoustic wave propagation within the cavity. Figure 1 illustrates the geometric parameters where the cavity depth is L and radius, a. The shaded region in the diagram represent the location of the acoustically transparent mesh. With the exception of the mesh, the walls can be modeled as either hard walls, 100% reflective, or soft walls with a frequency dependent impedance. The pressure fluctuations from the TBL along the top of the cavity were initially modeled using a wavelet expression for boundary layer pressure waves. Additionally, wall pressure spectra models from literature were used as inputs to this expression. The propagation of acoustic waves within the cavity is calculated by solving the wave equation [14], eq. 1, where p is the pressure, t is time, and c_0 is the speed of sound in air by satisfying the boundary conditions that define the cavity.

$$\frac{\partial^2 p}{\partial^2 t} - c_0^2 \nabla^2 p = 0 \tag{1}$$

The boundary conditions describe the velocity and pressure changes at the cavity walls, at the bottom of the cavity, and across a mesh at the top of the cavity. Additionally, an expression for the boundary layer pressure fluctuations was imposed at the top of the cavity, above the mesh. It is assumed that the energy content of the pressure fluctuations within the boundary layer is fully converted in the associated acoustic wave. The resulting solutions are used to describe the pressure field in the cavity and evaluate the reduction in spectral energy at the bottom of the cavity.

A. Cavity Boundary Conditions

In order to solve the wave equation, eq. 1, the cavity boundary conditions for pressure and velocity need to be defined [15]. The porous mesh is represented by imposing a pressure jump across the material with a specified resistance. The model allows for both hard and soft cavity walls to be incorporated [16]. The model can be used to estimate the acoustic pressure and velocity at all locations within the 3D cavity. However, of primary interest is the comparison between the integrated calculated pressure along the top of the cavity and at the bottom of the cavity.

A sketch illustrating the boundary conditions can be seen in figure 1. In this figure, the shaded area represents the mesh. The cavity is defined in terms of cylindrical coordinates, r, θ, and z. In order to simplify calculations, the fluid properties and geometric variables are normalized so that $\tilde{p}$, $\tilde{\rho}$, $\tilde{v}$, $\tilde{\omega}$, $\tilde{r}$, $\tilde{t}$, and $\tilde{z}$ represents the normalized values for pressure, density, velocity, angular frequency, radius, time, and propagation distance respectively.

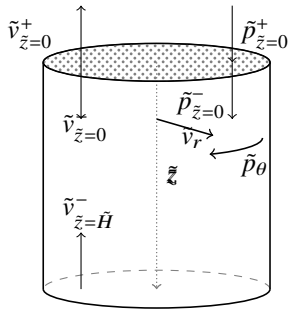

Fig. 1 Model geometry and boundary conditions

The first radial boundary condition at the cavity center line, $\tilde{r} = 0$, is expressed by eq. 2, where $\tilde{v}_{\tilde{r}}$ is the radial velocity. At $\tilde{r} = 0$, the acoustic particle velocity must have a finite value [6].

$$\tilde{v}_{\tilde{r}}|_{\tilde{r}=0} = finite \tag{2}$$

The velocity at the wall, $\tilde{r} = 1$, depends on whether or not the cavity has hard or soft walls. Equation 3 states that the radial velocity must equal zero in the direction normal to the walls for hard walls.

$$\tilde{v}_r|_{\tilde{r}=1} = 0 \tag{3}$$

The velocity is proportional to the partial derivative of pressure with respect to $\tilde{r}$ at $\tilde{r} = 1$ [8], as shown in eq. 4. In this equation, Z is the dimensionless wall impedance and $\tilde{\omega}$ is the angular frequency. The definition of impedance is the change in pressure divided by its acoustic velocity [8]. For the case of hard walls, $Z = \infty$, which results in the right hand side being equal to zero.

$$\left.\frac{\partial \tilde{p}}{\partial \tilde{r}}\right|_{\tilde{r}=1} = -\frac{i\tilde{\omega}\tilde{p}}{Z} \tag{4}$$

If the walls are made of a lining material, such as melamine foam, as described in Allard and Daigle [16], this expression instead of being equal to zero, as in eq. 3, is inversely proportional to the impedance of the soft wall.

Along the z direction, boundary conditions are defined at the bottom of the cavity and at the top. Equation 5 expresses that the velocity, $\tilde{v}_{\tilde{z}}$, is zero at the bottom of the cavity for the case of a hard wall.

$$\tilde{v}_z|_{\tilde{z}=\tilde{L}} = 0 \tag{5}$$

For the soft wall case, a reflection coefficient for the ratio between the incident and reflected pressure waves at $\tilde{z} = \tilde{H}$ must be defined [17]. This expression is given in eq. 6, where Z_s is the normalized surface impedance, the impedance of the material upon 90° incident waves, at the bottom of the cavity.

$$R_{refl} = \frac{Z_s - 1}{Z_s + 1} \tag{6}$$

The effect of the mesh is modeled by imposing a boundary condition for the velocity and the pressure jump across the material. It is assumed that the acoustic velocity in the z-direction is equal on either side of the material, as represented by equation 7.

$$\tilde{v}_z^+|_{\tilde{z}=0} = \tilde{v}_z^-|_{\tilde{z}=0} \tag{7}$$

The change in pressure across the mesh is derived from an estimated impedance across the porous material. For this model it is assumed to be equal to the characteristic specific acoustic impedance ($\rho_0 c_0$) multiplied by a dimensionless acoustic resistance term, R, as shown in equation 8.

$$\frac{\tilde{p}^-|_{\tilde{z}=0} - \tilde{p}^+|_{\tilde{z}=0}}{\tilde{v}_z|_{\tilde{z}=0}} = R \tag{8}$$

The final boundary condition for this model is for the pressure in the circumferential direction [17]. Equation 9 shows that the pressure at $\theta = 0$ must not have a discontinuity at $\theta = 2\pi$.

$$\tilde{p}(\tilde{r}, \theta, \tilde{z}) = \tilde{p}(\tilde{r}, \theta + 2\pi, \tilde{z}) \tag{9}$$

B. Modeling turbulent boundary layer pressure spectral energy

The boundary layer acoustic pressure fluctuations are assumed to vary along the top of the cavity, where $z = 0$. In order to describe these fluctuations, an expression in the spatial wave number domain was developed as shown in equation 10. The pressure signal varies with respect to time, t, wave number, $k = \frac{\omega}{U_c}$, U_c the convection speed of the boundary layer, σ, a wavelet expression constant, and x_0, an arbitrary initial value.

$$p(k,t) = \int_{-\infty}^{\infty} p(x,t)\, dx = \frac{\sigma U_c \sqrt{\pi}}{\omega} e^{i(\omega t + k_x x_0)} \left(1 - e^{-\frac{\sigma^2}{2}\left(1 + \frac{k_x U_c}{\omega}\right)^2}\right) \tag{10}$$

Equation 10 is dependent on the boundary layer convective velocity to define the coherence length. Boundary layer acoustic wave amplitudes are dependent on σ, similar to the approach introduced by Corcos [9]. This expression is the

Dirichlet boundary condition for pressure at $z = 0$, the interface of the cavity with the boundary layer. This equation was modified so that instead of having the TBL pressure amplitudes defined by σ, wall pressure spectral models were used to define the amplitude.

$$\tilde{p}\left(\tilde{r}, \theta, 0\right) = \frac{\sqrt{\Phi\left(\omega\right)}}{\rho_0 c_0^2} \Delta\omega e^{\frac{-i\omega}{U_c}\tilde{r}(\cos(\theta))} \tag{11}$$

Equation 11, where $\Phi\left(\omega\right)$ is the spectral energy, ρ_0 is the characteristic density of air, c_0 is the characteristic speed of sound in air, $\tilde{r}$ is the normalized radial position across the top of the cavity, θ is the azimuthal position on the top of the cavity. This equation was developed along the same principles of eq. 10 to allow for mode matching [8] the boundary layer pressure spectra with the acoustic modes. The details of which will be discussed later. The following boundary layer wall pressure models were evaluated with eq. 11:

$$\frac{\Phi\left(\omega\right) U_e}{\tau_w^2 \delta^*} = \frac{2\left(\omega\delta^*/U_e\right)^2}{\left[\left(\omega\delta^*/U_e\right)^2 + 0.0144\right]^{1.5}} \tag{12}$$

Equation 12 is the Howe model for boundary layer spectral energy, where U_e is the boundary layer velocity, δ^* is the boundary layer displacement thickness, and τ_w is the wall shear stress.

$$\Phi\left(\omega\right) = \frac{5.1\left(\tau_w^2 \delta^*/U_\infty\right)}{\left[1 + 0.44\left(\omega\delta^*/U_\infty\right)^{7/3}\right]} \tag{13}$$

Equation 13 is the Smol'yakov and Tkachenko model, where U_∞ is the free stream velocity.

$$\frac{\Phi\left(\omega\right) U_e}{\tau_w^2 \delta} = \frac{3\left(\omega\delta/U_e\right)^2}{\left[\left(\omega\delta/U_e\right)^{0.75} + 0.5\right]^{3.7} + \left[\left(1.1R_T^{-.057}\right)^{0.75}\left(\omega\delta/U_e\right)\right]^7} \tag{14}$$

Equation 14 is the Goody model, where R_T is the time scale ratio defined as $\left(u_*\delta/\nu\right)/\sqrt{c_f/2}$. In this expression, c_f is the skin friction coefficient, u^* is the friction velocity, and ν is the kinematic viscosity.

These boundary layer models assume that it is acting upon a hard wall [18]. However, the cavity model assumes that acoustic velocity through the mesh above the cavity is allowed. This simplification is intended to allow for the study of how the TBL noise attenuates through the cavity and is not intended to fully represent the boundary layer flow phenomena over a porous material. Additionally, it is assumed that due to the presence of a mesh, that there is no flow into the cavity and that the only flow within the cavity is due to the acoustic waves transmitted through the mesh. The Smol'yakov and Tkachenko boundary layer model was chosen as input to the cavity model as it better matched the experimental data used for validating the model.

C. Solution to the wave equation

The wave equation is solved by separation of variables. With the previously defined boundary conditions, it is now possible to solve the wave equation, eq. 1 by using separation of variables [15, 17]. The sound pressure field solutions will be in the form of the generic equation 15 where $F\left(\tilde{r}\right)$, $G\left(\theta\right)$, and $H\left(\tilde{z}\right)$ are solutions to their respective ordinary differential equations.

$$\tilde{p}\left(\tilde{r}, \theta, \tilde{z}, \tilde{t}\right) = e^{i\tilde{\omega}\tilde{t}} F\left(\tilde{r}\right) G\left(\theta\right) H\left(\tilde{z}\right) \tag{15}$$

Equation 15 is substituted into the wave equation to get a three dimensional partial differential equation, eq. 16. This expression is made up of independent ordinary differential equations that equal a constant [15].

$$-k^2 - \frac{G''\left(\theta\right)}{\tilde{r}^2 G\left(\theta\right)} - \frac{H''\left(\tilde{z}\right)}{H\left(\tilde{z}\right)} - \frac{F''\left(\tilde{r}\right)}{F\left(\tilde{r}\right)} - \frac{F'\left(\tilde{r}\right)}{\tilde{r}F\left(\tilde{r}\right)} = 0 \tag{16}$$

This procedure results in eqs. 17, 18, and 19 where α represents the radial wave number, m the azimuthal mode number, and k the axial wave number [8].

$$-\frac{F''\left(\tilde{r}\right)}{F\left(\tilde{r}\right)} - \frac{F'\left(\tilde{r}\right)}{\tilde{r}F\left(\tilde{r}\right)} - \alpha^2 = \frac{m^2}{\tilde{r}^2} \tag{17}$$

$$\frac{G^{''}(\theta)}{G(\theta)} = m^2 \tag{18}$$

$$\frac{H^{''}(\tilde{z})}{H(\tilde{z})} = \alpha^2 - k^2 \tag{19}$$

Equation 17 has a solution in the form of a generic Bessel function, seen in eq. 20, where $J_m(\xi\tilde{r})$ is a Bessel function of order m of the first kind and $Y_m(\xi\tilde{r})$ is a Bessel function of order m of the second kind.

$$F(\tilde{r}) = A_r J_m(\xi\tilde{r}) + B_r Y_m(\xi\tilde{r}) \tag{20}$$

The boundary conditions, eqs. 2 and 3 are applied to eq. 20. Since the solution of eq. 20 must exist and $Y_m(\xi\tilde{r})$ is infinite at $\tilde{r} = 0$, B_r must equal zero to satisfy eq. 2. For the hard wall case, velocity is zero at the wall, $\tilde{v}_r|_{\tilde{r}=1} = 0$, therefore $J_m^{'}(\xi\tilde{r}) = 0$. The eigenvalue of this equation is the radial wave number, $\alpha_{m\mu}$, which is equal to $\xi\tilde{r}$. Each eigenvalue of $J_m^{'}(\alpha_{m\mu}) = 0$ is referenced by the symbol μ.

For the soft wall case, the boundary condition eq. 4 is applied, which results in eq. 21.

$$\frac{J_m(\alpha_{m\mu})}{\alpha_{m\mu} J_m^{'}(\alpha_{m\mu})} = \frac{iZ}{\omega} \tag{21}$$

The resulting eigenvalue, the radial wave number, is now complex valued but is close to the value of the hard walled radial wave number.

The solution for F is normalized by $N_{m\mu}$, defined in eq. where $N_{m\mu}$ is chosen so that it scales with the energy content of the corresponding mode. [17].

$$N_{m\mu} = \begin{cases} \sqrt{2}, & \text{for } m = 0 \;\&\; \mu = 1 \\ \dfrac{\sqrt{2}}{J_m(\alpha_{m\mu})\sqrt{\left(1 - \frac{m^2}{\alpha_{m\mu}^2}\right)}}, & \text{all other values} \end{cases} \tag{22}$$

The final form of the solution to F is shown in eq. 23.

$$F_{m\mu}(r) = N_{m\mu} J_m(\alpha_{m\mu}\tilde{r}) \tag{23}$$

The solution for $G(\theta)$, eq. 18, must be periodic per the boundary conditions, eq. 9, since the solutions at $\theta = 0$ and $\theta = 2\pi$ are equal. Equation 24 is the solution where $m = 0, \pm1, \pm2, \ldots \infty$.

$$G_m(\theta) = e^{-im\theta} \tag{24}$$

The solution to the differential equation, $H(\tilde{z})$, eq. 19, for the wave propagation in the axial direction is shown by eq. 25. $A_{m\mu}$ and $B_{m\mu}$ are the modal amplitudes, where $k_{m\mu}$ is the axial wave number. $A_{m\mu}$ is the inward propagating mode and $B_{m\mu}$ is the outward propagating mode.

$$\begin{cases} H_{m\mu}(\tilde{z}) = A_{m\mu}^{+} e^{ik_{m\mu}\tilde{z}} + B_{m\mu}^{+} e^{-ik_{m\mu}\tilde{z}}, & \tilde{z} < 0 \\ H_{m\mu}(\tilde{z}) = A_{m\mu}^{-} e^{ik_{m\mu}\tilde{z}} + B_{m\mu}^{-} e^{-ik_{m\mu}(\tilde{z}-\tilde{L})}, & \tilde{z} > 0 \end{cases} \tag{25}$$

Given that the mesh introduces a discontinuity, the solution is split across the mesh because modal amplitudes are not equal. The modes just above the mesh are denoted by the + superscript while the modes below the mesh are denoted by the − superscript. Figure 2 illustrates the location and direction of propagation of these modes. Equation 26 defines the axial wave number, $k_{m\mu}$ [8].

$$k_{m\mu} = -sign\left(\Im\left(\sqrt{\tilde{\omega}^2 - \alpha_{m\mu}^2}\right)\right)\sqrt{\tilde{\omega}^2 - \alpha_{m\mu}^2} \tag{26}$$

The axial wave number at a given angular frequency defines if a mode, (m, μ), is cut-on or cut-off. A mode is cut-on if $k_{m\mu}$ is real which will result in the acoustic wave energy being propagated [14] to the bottom of the cavity. Cut-off

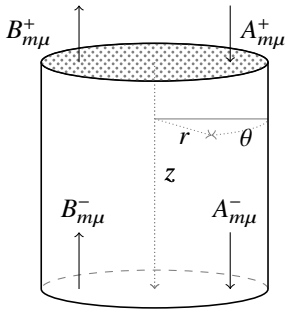

Fig. 2 Model coefficients

modes have imaginary axial wave numbers, which results in the energy decaying exponentially. This is the primary mechanism for the attenuation of the TBL acoustic waves within the cavity.

It is now possible to determine a system of equations for three of the four modal amplitude coefficients. The system of equations is calculated by applying the boundary conditions, eqs. 5, 7, and 8 to the expressions for the pressure, eq. 15, and velocity, eq. 27. The velocity field is calculated using eq. 27.

$$\tilde{v}_z\left(\tilde{r},\theta,\tilde{z},\tilde{t}\right) = -\int \frac{\partial \tilde{p}}{\partial \tilde{z}} \partial \tilde{t} = -\frac{k_{m\mu}}{i\tilde{\omega}} e^{i\tilde{\omega}t} F\left(\tilde{r}\right) G\left(\theta\right) H^{'}\left(\tilde{z}\right) \tag{27}$$

The solutions for the pressure and velocity are determined by substituting the solutions to the differential equations, eqs. 23 - 25 into the general equations for pressure and velocity. Equation 28 is the result of applying the boundary conditions, eqs. 3, 4, 5, 7, and 8 to the solutions.

$$\begin{aligned} R_{refl} A^-_{m\mu} e^{-ik_{m\mu}\frac{H}{a}} - B^-_{m\mu} &= 0 \\ A^+_{m\mu} - B^+_{m\mu} &= A^-_{m\mu} - B^-_{m\mu} e^{-ik_{m\mu}\tilde{L}} \\ A^-_{m\mu} + B^-_{m\mu} e^{-ik_{m\mu}\frac{H}{a}} - A^+_{m\mu} - B^+_{m\mu} &= -R\frac{k_{m\mu}}{\tilde{\omega}}\left[A^+_{m\mu} - B^+_{m\mu}\right] \end{aligned} \tag{28}$$

The fourth coefficient, $A^+_{m\mu}$, is calculated by mode matching [8] the pressure fluctuations from the boundary layer model with that of the pressure field in the cavity (equation 15) just above the mesh. This results in $A^+_{m\mu}$ being equal to the integral of the mode matched pressure expressions across the interface as shown in equation 29.

$$A^+_{m\mu} = \frac{1}{2\pi}\int_0^{2\pi}\int_0^1 \tilde{p}\left(\tilde{r},\theta,0\right) F_{m\mu}(\tilde{r}) e^{im\theta}\tilde{r}\, d\tilde{r}\, d\theta \tag{29}$$

The normalized pressure term in eq. 29 is defined by eq. 11, where $\Phi\left(\omega\right)$ is the spectral energy density calculated by the boundary layer models, eqs. 12 - 14.

In order to validate this model with experimental data, the spectral energy needs to be calculated from the resulting modal amplitudes. Equation 30 calculates the spectral energy at the top of the cavity, $\tilde{z} = 0$.

$$P = \left|A^+_{01}\right|^2 + \frac{1}{2}\sum_{m=-\infty}^{\infty}\sum_{\mu=1}^{\infty}\left|A^+_{m\mu}\right|^2 \tag{30}$$

At the bottom of the cavity for $z = H$, $G_{m\mu}\left(H\right) = 2B^-_n$. The resulting integrated pressure at the bottom of the cavity is calculated using eq. 31.

$$Q = 4\left|B^-_{01}\right|^2 + 2\sum_{m=-\infty}^{\infty}\sum_{\mu=1}^{\infty}\left|B^-_{m\mu}\right|^2 \tag{31}$$

D. Model Implementation

This system of equations described in eq. 28 is solved iteratively. For the first iteration, $A^+_{m\mu}$ is calculated from eq. 29. During this iteration step when solving eq. 28 it is assumed that $B^-_{m\mu} = 0$. Then the second equation is rearranged

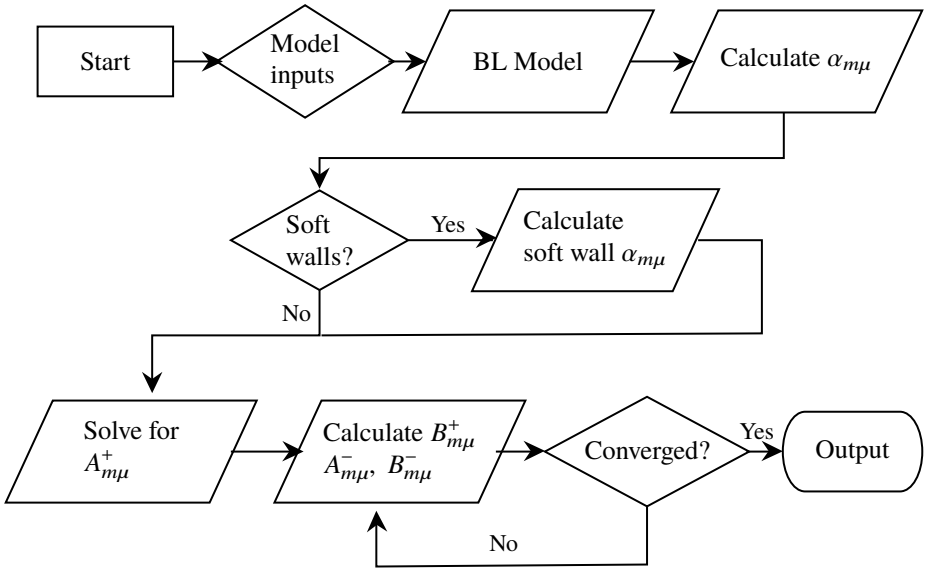

Fig. 3 Model implementation flow diagram

Table 1 Tunnel velocity at which data were collected

Tunnel	Velocity (m/sec)
LTT & DWG	30.0
LTT & DWG	50.0
DWG	60.0
LTT	70.0

into terms of $A^-_{m\mu}$ and substituted into the third, in order to solve for $B^+_{m\mu}$. This gives the initial values for the modes. For the subsequent iterations, the value of equation $A^-_{m\mu}$ from the previous iteration loop was used in eq. 28 to determine $B^-_{m\mu}$. The remaining coefficients are then calculated. Iteratively solving the coefficients continues until the error term is less than 1×10^{-40}. Error is defined as follows: $\left|\sum \left|B^{(n)-}_{m\mu}\right| - \sum \left|B^{(n-1)-}_{m\mu}\right|\right|$ which is the difference between the absolute value of the sum of all values of $B_{m\mu}$ at the current iterative step and the previous one. This process needs to be repeated at each frequency of interest.

Figure 3 provides a high level overview of the implemented model. The model inputs include the boundary layer parameters and state variables. These are used for the models in eqs. 12 - 14 with the desired boundary layer model which is also an input parameter. Additional model parameters include the frequency at which to calculate the wave propagation in the cavity, whether the cavity has hard or soft walls, the desired error term, and the number of modes to calculate a solution.

IV. Experimental Details

Two test campaigns were conducted to collect the data used to validate the cavity model. The first test occurred in January 2018 where 12 cavity geometries were tested in the LTT wind tunnel at TU Delft. More details on this test can be found in reference [13]. The second test occurred in June 2018 at the Deutsche WindGuard (DWG) wind tunnel in Bremerhaven, Germany. The objective of this test was to establish baseline measurements to quantify the cavity performance as well as the acoustic properties of the wind tunnel itself. For the cavity measurements, the existing cavities designed by Deutsche WindGuard were used. Table 1 provides an overview of the tunnel speeds at which data were collected. For comparing experimental data with the model, only the 30 m/sec cases were used.

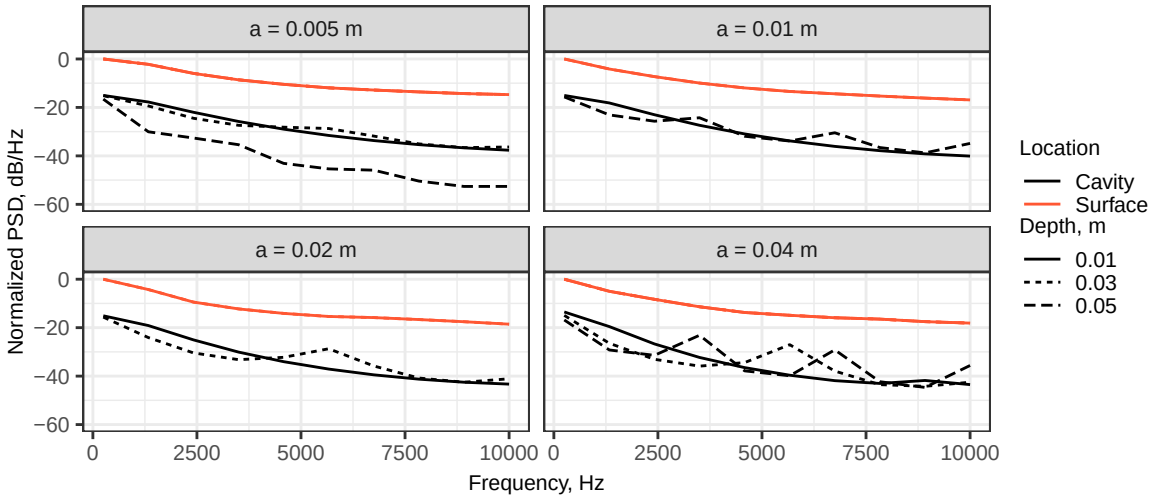

Fig. 4 Initial model results, velocity = 30 m/sec, modeled acoustic resistance R = 2, boundary layer modeled with Smol'yakov and Tkachenko model. The four subplots show the results for cavities with radii: a = 0.005 m, a = 0.01 m, a = 0.02 m, a = 0.04 m.

Two cavity geometries are compared against the model. The cavity placed in the LTT, is a stainless steel mesh (200 threads per cm) covering a cylindrical cavity with a diameter of 1 cm and a depth of 1 cm. It was tested in the LTT wind tunnel. Deutsche WindGuard's cavity is a proprietary design but features a conical shape, a stainless steel mesh, and absorptive material within the cavity. Currently the model does not account for variable diameters along the cavity depth. Future iterations will model the effect of variable diameter. Both experiments used LinearX M51 microphones to measure the hydrodynamic fluctuations along the wall and in the cavity. M51 microphones are condenser microphones with a dynamic range of 122 dB up to 20 kHz with an error of ±1 dB.

V. Results

The model estimated the power spectral density (PSD) at the top of the cavity based on the the boundary layer models used as input as previously discussed. This was compared against the power spectral density at the bottom of the cavity, estimated by propagating the acoustic waves from the top to the bottom of the cavity. Twenty different cavity geometries were modeled, half of which had hard reflecting walls and the other half had soft walls at the bottom and sides. The radii of the cavities were 0.005 m, 0.01 m, 0.02 m, and 0.04 m. The cavity depths were 0.01 m, 0.03 m, and 0.05 m. The model was then compared against the experimental data for two different cavity geometries. The model trends agreed with prior experimental data [13].

A. Hard Wall Results

A comparison between the integrated pressure at the top and bottom of the cavities for the hard wall case is shown in figure 4. The magnitude of the power spectral density is seen to decrease with increasing cavity depth. This is due to the majority of acoustic modes being cut-off. As example, fig. 5 shows the axial wave numbers for two cases, a cavity with $a = 0.005$ m at a low frequency, and a cavity with a larger radius, $a = 0.04$ m and at a higher frequency. As discussed previously with eq. 26, cut-off modes have an imaginary axial wave number, $k_{m\mu}$. For the first case, all modes but the plane wave mode ($m = 0$, $\mu = 1$) are cut-off which means that the acoustic energy decays more rapidly with distance, per eq. 25. This figure also shows that for a larger cavity, more modes at higher frequencies are cut-on, which means less attenuation. This is why fig. 4 shows less reduction in acoustic energy at higher frequencies with respect to increasing cavity depth. Figure 6 shows the modal distribution of the boundary layer energy, represented by $A^{+}_{m\mu}$. As this figure shows, for lower frequencies, fig. 6a, most energy is concentrated in the $m = 0$ and $\mu = 1$ mode, the plane wave. For higher frequencies, fig. 6b, it is spread out across more azimuthal cut-on modes, $m = 1$ and $m = 2$ (with $\mu = 1$). This is why at higher frequencies, more energy is transmitted to the bottom of the cavity, reducing the effect of cavity depth.

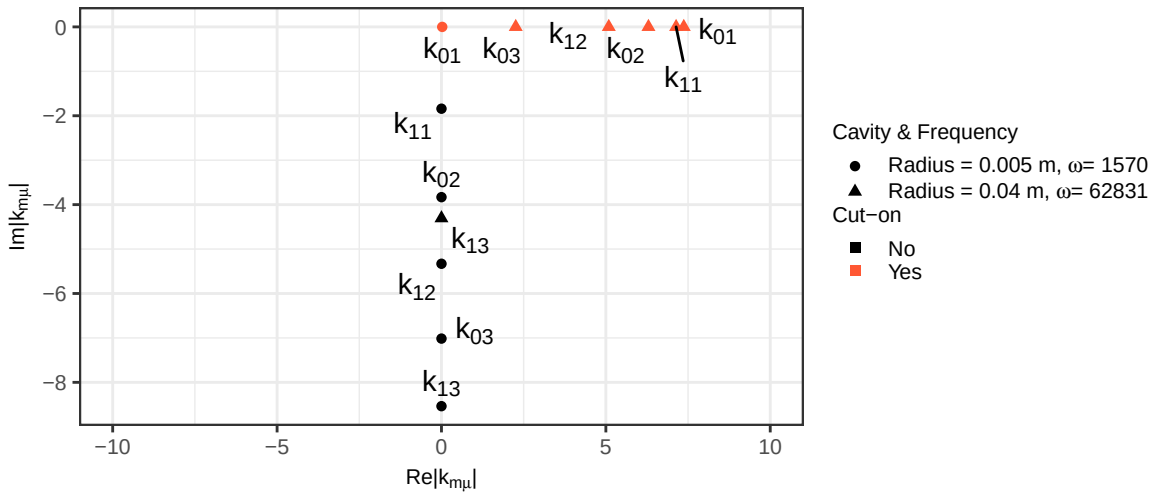

Fig. 5 Comparison of axial wave numbers, $k_{m\mu}$, with cut-on and cut-off values for a cavity with a = 0.005 m, ω = 1570 and a cavity with a = 0.04 m, ω = 62831

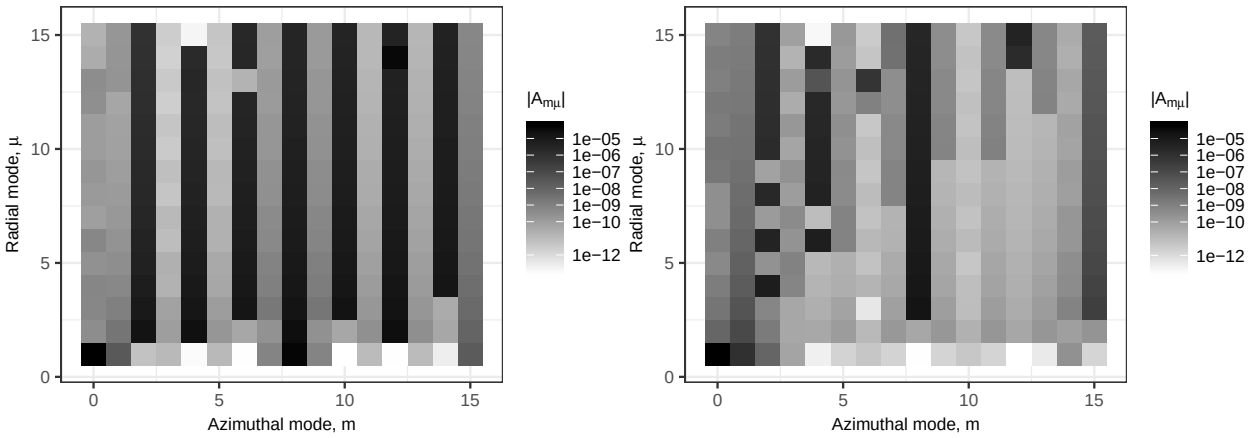

Fig. 6 Modal distribution of acoustic energy for the boundary layer, $A^{+}_{m\mu}$ at two angular frequencies. (a) Low frequency, ω = 1570. (b) Higher frequency, ω = 62831.

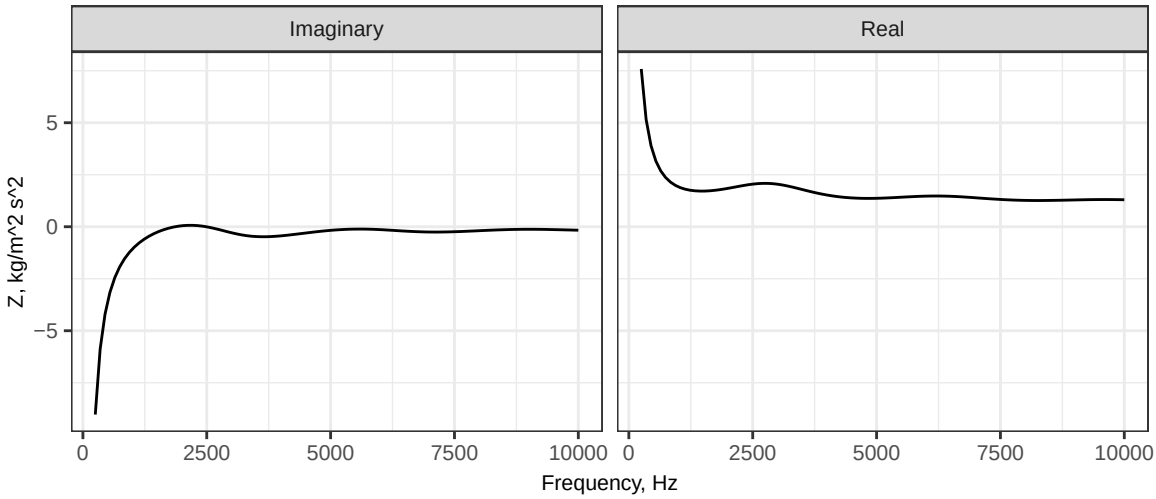

Fig. 7 Modeled impedance of Melamine Foam

Table 2 Radial wave number comparison for hard and soft walls for m = 0, $\tilde{\omega}$ = 0.0684, a = 0.005 m

μ	$\alpha_{m\mu}$ Hard	$\alpha_{m\mu}$ Soft
1	3.8317	3.8291+0.0016i
2	7.0156	7.0141+0.0009i
3	10.1735	10.1725+0.0006i
4	13.3237	13.3230+0.0004i

The reduction in acoustic energy from the top to the bottom of the cavity is the same order of magnitude as prior experimental measurements [13]. With respect to cavity diameter, the model shows that increasing the diameter of the cavity slightly decreases the spectral energy at the bottom of the cavity by 5 dB at 10 kHz. This is shown by comparing the 0.04 m diameter cavity to the 0.005 m diameter cavity for a depth of 0.01 m in fig. 4. During the LTT experiments [13], cylindrical cavities with the diameters that ranged from 1 cm to 0.5 cm were tested. These measurements also showed the spectral energy decreasing with increasing diameter. The trend of increasing divergence with frequency matches the experimental data. For the larger cavities, resonant modes appear in the model. Since these geometries were not tested, it is not possible to confirm if the model predicts resonances at the same frequencies.

B. Soft Wall Results

For the soft wall case, the walls were modeled as a melamine foam. The MLULb2016 model was used [19]. Figure 7 shows the resulting output of the impedance model. The radial wave numbers for the soft wall case were calculated by solving eq. 21. For the soft wall case, they are complex valued but close to the hard wall values [8]. This is shown in table 2.

The model results for the soft wall case are plotted in fig. 8. As shown in this figure, the melamine walls result in a substantial reduction in acoustic energy by 15 dB as shown in fig. 9. The melamine foam attenuates the resonance seen for the hard wall case in fig. 4 as well as reducing the influence of cavity depth. Presumably this is due to the soft walls absorbing up to 90% of the reflected energy which is more than the energy attenuated with increasing the distance the evanescent wave travels due to the deeper cavity. This is why changing depth has much less of an effect of the reduction in acoustic energy at the base of the cavity. Increasing cavity diameter slightly reduces the acoustic energy at the bottom of the cavity. The majority of reduction in acoustic energy is due to the softwall at the bottom of the cavity. When the bottom of the cavity was modeled as a hard surface, the soft walls only reduced the acoustic energy by 0.3 dB.

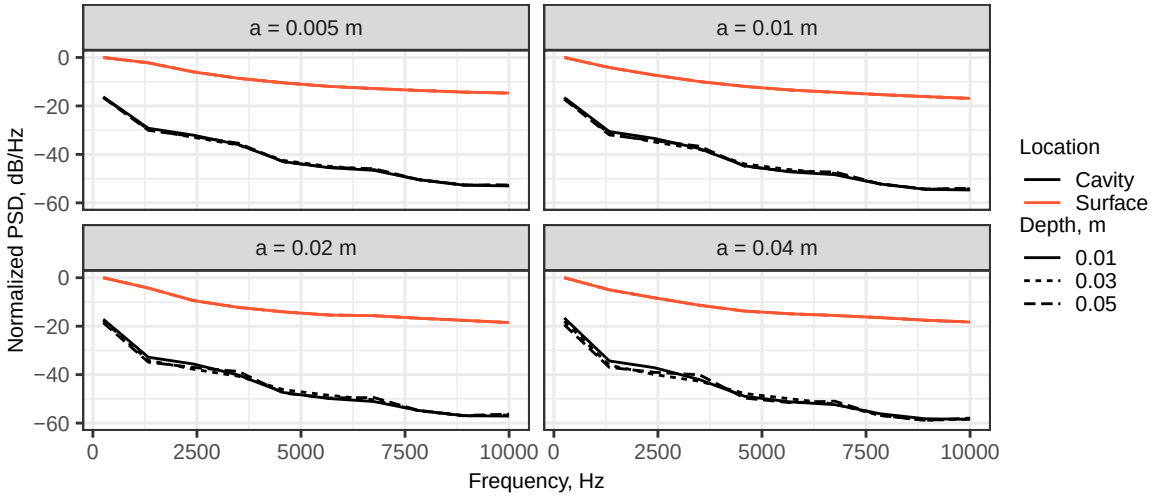

Fig. 8 Soft Wall Model Results, velocity = 30 m/sec, modeled acoustic resistance R = 2, boundary layer modeled with Smol'yakov and Tkachenko model

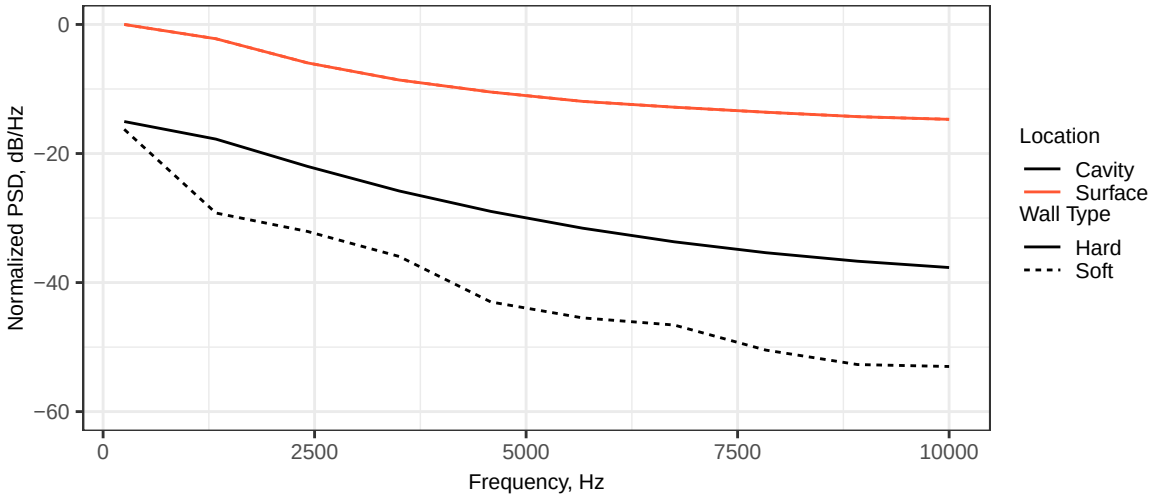

Fig. 9 Comparison of Hard and Soft Wall Model Results, velocity = 30 m/sec, modeled acoustic resistance R = 2, radius = 0.005 m, depth = 0.01 m, boundary layer modeled with Smol'yakov and Tkachenko model

C. Comparison to Experimental Data

This model is currently limited to three dimensional, straight walled geometries that can have hard or soft walls. The cavities used in the LTT measurement campaign featured hard wall cavities with both constant diameters and varying ones. The DWG campaign featured their proprietary cavity design that features soft walls and a varying diameter. The measured boundary layer spectral energy from the LTT and DWG campaigns was used as input to the previously described model. Figure 10, compares the output of the model with these experiments performed on two cavities in the two wind tunnels. The cavity tested in the LTT had a depth of 1 cm and a radius of 0.5 cm cylinder, tested at 30 m/sec. The model captures the approximate 20 dB change in the power spectra between the top of the cavity and the bottom reasonably well. However it does not capture the frequency dependence perfectly. At low frequencies, the measurements are close to each other and diverge with increasing frequency. The peak at 6 kHz is not seen in the model and is possibly being excited by a process that is not modeled.

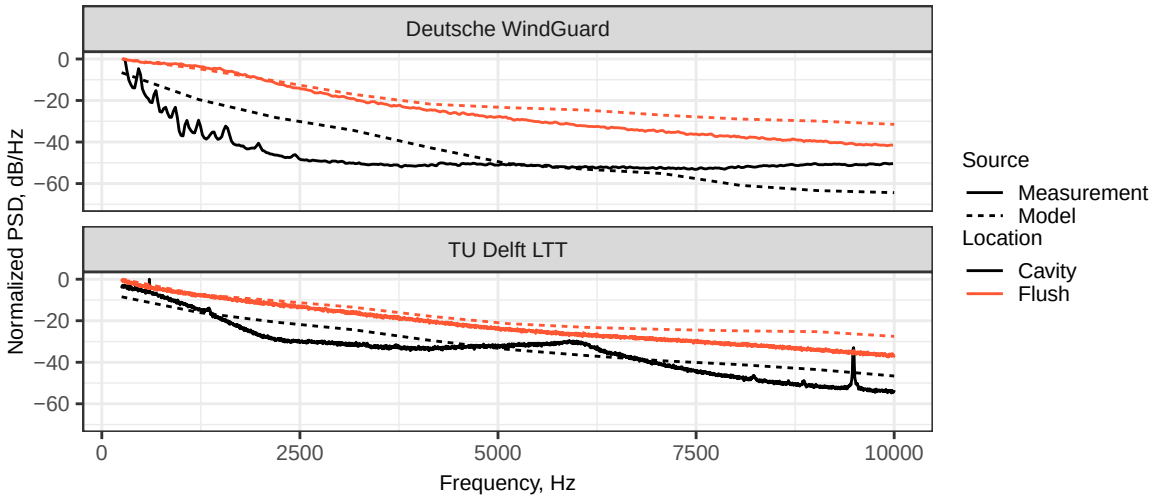

Fig. 10 Comparison to experimental data, velocity = 30 m/sec, modeled acoustic resistance R = 2, experimental spectral data used as input to the model

For the comparison with the DWG cavity, a cavity with the same diameter and depth with melamine foam walls was modeled. However, since the model is not yet capable of modeling change in diameter, it does not perfectly match the DWG design. Despite these simplifications to the model, it did a reasonable job of predicting the reduction in spectral energy. The frequency dependence is more in line with the measurements, especially between 0.25 kHz and 5 kHz. The impedance of the material used to line the DWG cavities is not precisely known so the MLULb2016 model was used [19]. These results show that the model predicts the trend in reduction of boundary layer pressure fluctuations at the bottom of the cavity. One potential explanation for the difference between experimental and model results is that the experimental data also includes hydrodynamic waves which are not captured by this model.

VI. Conclusions

This paper describes the development of a deterministic model for predicting the attenuation of boundary layer pressure fluctuations within a cylindrical cavity. This model applies the methods for solving the wave equation within a duct to that of a cavity. A porous material covering the interface between the cavity and the boundary layer is also modeled. This model uses boundary layer spectral estimates from either the Howe model [10], the Smol'yakov and Tkachenko model [11], and the Goody Model [12] as well as experimental data as input to the model. Both reflecting hard walls and walls with an acoustic absorbing liner were evaluated. The primary physical mechanism for the attenuation of boundary layer pressure fluctuations was that for the modeled small cavities, the majority of acoustic modes are cut-off which results in exponential reduction in acoustic energy with cavity depth. This model was shown to predict the reduction in boundary layer noise at the bottom of the cavity over a range of frequencies and geometries in reasonable agreement with experimental data given the model constraints.

In order to better understand how to leverage the cavity design to improve aeroacoustic measurements, having a

physics based model is critical. This allows for design decisions regarding the shape and material of cavities to be made in a logical manner. By knowing a priori which designs show promise to reduce background turbulent boundary layer noise, resources can be better utilized. This means that time can be saved by only performing detailed computational fluid dynamic simulations and experiments on designs whose improvements have a physical basis. However, in order to get to this point this model needs to be validated and be capable of modeling a sufficient amount of design parameters such as materials, cavity shapes, and the influence of different boundary layer parameters.

In the near term the focus of this research will be to expand the capabilities of this model. It is important to accurately model non-constant diameters as the change in diameter will further reduce the spectral energy in the cavity [8, 13, 20–23]. Further work will also be done to improve the boundary conditions of this model. This model will be used as a tool to support future studies with finite element modeling and Lattice Boltzman based CFD solvers for wave propagation in more complex cavities.

Acknowledgments

The authors would like to acknowledge the Applied and Engineering Sciences (TTW) branch of the Netherlands Organisation for Scientific Research (NWO) for funding the THAMES project. Additionally, the authors would like to thank Deutsche WindGuard for their support and access to their facilities.

References

[1] Sijtsma, P., "Phased Array Beamforming Applied to Wind Tunnel And Fly-Over Tests," *SAE Technical Paper Series*, Vol. 1, 2011, p. 49. doi:10.4271/2010-36-0514.

[2] Radhakrishnan, S., and Vakili, A., "Acoustic measurements and background noise separation in wind tunnels," *5th AIAA/CEAS Aeroacoustics Conference and Exhibit*, American Institute of Aeronautics and Astronautics, Reston, Virigina, 1999, pp. 1123–1132. doi:10.2514/6.1999-1990.

[3] Fleury, V., Coste, L., Davy, R., Mignosi, A., Cariou, C., and Prosper, J.-M. M., "Optimization of Microphone Array Wall Mountings in Closed-Section Wind Tunnels," *AIAA Journal*, Vol. 50, No. 11, 2012, pp. 2325–2335. doi:10.2514/1.j051336.

[4] Eversman, W., "Theoretical model for duct acoustic propagation and radiation," Tech. Rep. 11, NASA, jul 1991.

[5] Ovenden, N., Eversman, W., and Rienstra, S., "Cut-on Cut-off Transition in Flow Ducts: Comparing Multiple-scales and Finite-element Solutions," *10th AIAA/CEAS Aeroacoustics Conference*, American Institute of Aeronautics and Astronautics, Manchester, UK, 2004. doi:10.2514/6.2004-2945.

[6] Rona, A., "The Acoustic Resonance of Rectangular and Cylindrical Cavities," *Journal of Algorithms & Computational Technology*, Vol. 1, No. 3, 2007, pp. 329–356. doi:10.1260/174830107782424110.

[7] Tam, C. K. W., "Recent advances in computational aeroacoustics," *Fluid Dynamics Research*, Vol. 38, No. December 2005, 2006, pp. 591–615. doi:10.1016/j.fluiddyn.2006.03.006.

[8] Rienstra, S. W., *Fundamentals of Duct Acoustics*, November, Eindhoven University of Tecnology, 2015. URL `https://www.win.tue.nl/~sjoerdr/papers/VKI_Rienstra.pdf`.

[9] Corcos, G. M., "The structure of the turbulent pressure field in boundary-layer flows," *Journal of Fluid Mechanics*, Vol. 18, No. 03, 1964, p. 353. doi:10.1017/S002211206400026X.

[10] Howe, M. S., *Acoustics of Fluid–Structure Interactions*, Cambridge University Press, Cambridge, 1998. doi:10.1017/CBO9780511662898.

[11] Smol'yakov, A., and Tkachenko, V., "Model of a Field of Pseudosonic Turbulent Wall Pressure Fluctuations in Turbulent Boundary Layers," *Sov. Phys. (Acoustics)*, Vol. 37 (6), 1991, pp. 629–631.

[12] Goody, M., "Empirical Spectral Model of Surface Pressure Fluctuations," *AIAA Journal*, Vol. 42, No. 9, 2004, pp. 1788–1794. doi:10.2514/1.9433.

[13] VanDercreek, C. P., Majunath, P., Ragni, D., and Snellen, M., "Design and Evaluation of Microphone Cavity Geometries for Wind-Tunnel Acoustic Measurements," *AIAA Scitech 2019 Forum*, American Institute of Aeronautics and Astronautics, Reston, Virginia, 2019. doi:10.2514/6.2019-1580.

[14] Morse, P. M., and Ingard, K. U., *Theoretical acoustics*, McGraw-Hill, New York SE - xix, 927 pages illustrations 23 cm., 1968.

[15] Lord, N., and Strauss, W. A., "Partial Differential Equations: An Introduction," *The Mathematical Gazette*, Vol. 77, No. 479, 1993, p. 286. doi:10.2307/3619758, URL https://www.jstor.org/stable/3619758?origin=crossref.

[16] Allard, J., and Daigle, G., "Propagation of Sound in Porous Media: Modeling Sound Absorbing Materials," *The Journal of the Acoustical Society of America*, Vol. 95, No. 5, 1994, pp. 2785–2785. doi:10.1121/1.409801.

[17] Rienstra, S. W., and Hirschberg, A., *An Introduction to Acoustics*, 2018. URL https://www.win.tue.nl/~sjoerdr/papers/boek.pdf.

[18] Blake, W. K., "Essentials of Turbulent Wall Pressure Fluctuations," *Mechanics of Flow-Induced Sound and Vibration, Volume 2*, Vol. 2, Elsevier, 2017, pp. 81–177. doi:10.1016/B978-0-12-809274-3.00002-7.

[19] Allen, A. R., and Schiller, N., "Experimental evaluation of equivalent-fluid models for melamine foam," *New England NoiseCon-16 Revolution in Noise Control*, Providence, RI, 2016.

[20] Navfeh, A. H., and Telionis, D. P., "Acoustic Propagation in Ducts with Varying Cross Sections," *The Journal of the Acoustical Society of America*, Vol. 53, No. 1, 1973, pp. 372–372. doi:10.1121/1.1982657.

[21] Miles, J., "The Reflection of Sound due to a Change in Cross Section of a Circular Tube," *The Journal of the Acoustical Society of America*, Vol. 16, No. 1, 1944, pp. 14–19. doi:10.1121/1.1916257.

[22] Oppeneer, M., Rienstra, S. W., and Sijtsma, P., "Efficient Mode Matching Based on Closed-Form Integrals of Pridmore-Brown Modes," *AIAA Journal*, Vol. 54, No. 1, 2016, pp. 266–279. doi:10.2514/1.J054167.

[23] Smith, A., Ovenden, N., and Bowles, R., "Flow and geometry induced scattering of high frequency acoustic duct modes," *Wave Motion*, Vol. 49, No. 1, 2012, pp. 109–124. doi:10.1016/j.wavemoti.2011.07.006.